Delft University of Technology

Document Version
Final published version

Licence
CC BY

Citation (APA)
Lin, Y. C., Bannenberg, L., Navarathna, A., Kim, H. S., & Popovich, V. (2026). In-situ nanocrystalline oxide formation in zirconium carbide ultra-high temperature ceramic under oxygen scarcity. *Open Ceramics*, *28*, Article 101061. https://doi.org/10.1016/j.oceram.2026.101061

Important note
To cite this publication, please use the final published version (if applicable).
Please check the document version above.

Copyright
In case the licence states “Dutch Copyright Act (Article 25fa)”, this publication was made available Green Open Access via the TU Delft Institutional Repository pursuant to Dutch Copyright Act (Article 25fa, the Taverne amendment). This provision does not affect copyright ownership.
Unless copyright is transferred by contract or statute, it remains with the copyright holder.

Sharing and reuse
Other than for strictly personal use, it is not permitted to download, forward or distribute the text or part of it, without the consent of the author(s) and/or copyright holder(s), unless the work is under an open content license such as Creative Commons.

Takedown policy
Please contact us and provide details if you believe this document breaches copyrights.
We will remove access to the work immediately and investigate your claim.

This work is downloaded from Delft University of Technology.

Open Ceramics 28 (2026) 101061



Contents lists available at ScienceDirect

Open Ceramics

journal homepage: www.sciencedirect.com/journal/open-ceramics





In-situ nanocrystalline oxide formation in zirconium carbide ultra-high temperature ceramic under oxygen scarcity

Yun-Ching Lin [a,*], Lars Bannenberg [b], Amy Navarathna [b], Hyun-Sik Kim [c], Vera Popovich [d]

[a] Department of Aerospace Structures and Materials, Faculty of Aerospace Engineering, Delft University of Technology, Kluyverweg 1, Delft, 2629 HS, the Netherlands
[b] Department of Radiation Science and Technology, Faculty of Applied Sciences, Delft University of Technology, Mekelweg 15, Delft, 2629 JB, the Netherlands
[c] Department of Materials Science and Engineering, University of Seoul, Seoul, 02504, South Korea
[d] Department of Materials Science and Engineering, Faculty of Mechanical Engineering, Delft University of Technology, Mekelweg 2, Delft, 2628 CD, the Netherlands

ARTICLE INFO

Keywords:
Zirconium carbide
In-situ oxidation
Oxygen-limited oxidation
Nanocrystalline oxide
Phase transformation

ABSTRACT

Zirconium carbide exhibits remarkable thermal and mechanical resilience, making it a leading candidate for extreme applications. While its oxidation in oxygen-rich environments has been extensively studied, its behavior in oxygen-limited environments remains largely unexplored. To our knowledge, we present one of the first comprehensive in-situ study of ZrC under vacuum (5×10^{-2} Pa) over 400–800 °C, systematically tracking phase evolution under different isothermal and cooling temperatures. A nanocrystalline zirconia–carbon composite layer forms, producing a single-layer scale distinct from double-layer structure observed in high oxygen pressures. We also observe phase transformation in vacuum-grown scale upon cooling at approximately 400 °C, far below the transformation temperature of undoped bulk zirconia. These results reveal that oxygen-deficient environments do not fully inhibit oxidation at high temperatures. This study advances the mechanistic understanding of ZrC oxidation under oxygen-scarce environments, offering new insights into ZrC surface chemistry and its thermally grown oxide behavior.

1. Introduction

Zirconium carbide (ZrC) is a prominent ultra-high temperature ceramic distinguished by its exceptional thermal stability [1] and melting point approaching 3500 °C [2]. In addition to its high melting point, ZrC exhibits high hardness [3], good thermal conductivity [4,5], and chemical inertness [6], making it a promising candidate for applications in extreme environments, inclusive of aerospace propulsion [7], thermal protection systems [8], and advanced nuclear energy systems [9,10]. These attributes position ZrC as a key material for next-generation high-temperature technologies.

Despite its outstanding intrinsic stability, the susceptibility of ZrC to oxidation at elevated temperatures remains a critical limitation to its practical deployment [1,11,12]. Extensive studies have characterized its degradation behavior in oxygen-rich environments, where rapid oxide scale formation, cracking, and spallation occurs [13–18]. In contrast, oxygen-limited conditions have received comparatively little attention, as degradation of ZrC is often assumed to be minimal in such environments [19,20]. Consequently, its long-term behavior at elevated temperatures under oxygen-constrained environments remains insufficiently understood.

Many high-temperature service environments such as high-altitude flight, space systems, and certain vacuum processing conditions are characterized not by abundant oxygen but by low oxygen partial pressures typically below ~10^2 Pa and in some cases down to ~10^{-2} Pa [21]. Under these conditions, surface-adsorbed oxygen, residual oxygen species, or trace oxygen can play a critical role in governing oxide scale growth, phase stability, and morphological evolution. For example, in some high-temperature material systems, such as NiCrAl alloy, low oxygen pressures suppress and delay the formation of Cr_2O_3 and NiO, which promotes a continuous Al_2O_3 layer [22]. The variations in oxygen pressure significantly influence the rate of protective oxide layer formation and the relative extent of transient oxide development prior to the onset of diffusion-controlled growth. In chromia-forming stainless steel, oxide composition and substrate depletion are also directly tied to oxygen pressure. The lower the oxygen pressure, the closer the protective scale approaches pure chromia, driven by thermodynamic stability of Cr-rich corundum at low oxygen pressure [23]. These observations underscore the role of oxygen availability in governing the oxidation behavior and morphological evolution of high-temperature materials.

* Corresponding author.
E-mail address: Y.Lin-4@tudelft.nl (Y.-C. Lin).

https://doi.org/10.1016/j.oceram.2026.101061
Received 15 July 2026; Accepted 30 September 2026
Available online 30 September 2026
2666-5395/© 2026 The Author(s). Published by Elsevier Ltd on behalf of European Ceramic Society. This is an open access article under the CC BY license (http://creativecommons.org/licenses/by/4.0/).

However, the extent to which ZrC undergoes oxidation and the formation of thermally grown oxide under oxygen-scarce environments remain largely unexplored. In particular, it is unclear how ZrC responds to sustained heating under limited oxygen, and how the resulting oxide scales differ from those formed in oxygen-rich atmospheres. Addressing this knowledge gap is essential for reliably deploying ZrC in advanced high-temperature systems.

In this study, we investigate the oxidation behavior of high-density monolithic ZrC under low oxygen partial pressure using a combination of in-situ and ex-situ characterization techniques. We present the first comprehensive in-situ vacuum (5×10^{-2} Pa) oxidation study of ZrC with controlled temperature variations, including isothermal holding and cooling stages. The phase stability of thermally grown oxide scales is systematically examined as a function of cooling temperature. Furthermore, we provide a comparison between oxide scales formed under oxygen-deficient conditions and those developed in oxygen-rich environments, enabling a unified understanding of ZrC oxidation across a wide range of oxygen partial pressures.

This work aims to clarify the oxidation response of ZrC under oxygen-limited conditions and fill the longstanding gap in comprehensive in-situ oxidation studies conducted under vacuum environment with temperature variation for extended durations. By revealing how thermally grown oxides nucleate, evolve, and stabilize in oxygen-scarce environments over prolonged exposure, this study provides fundamental insight into ZrC oxidation mechanisms beyond conventional oxygen-rich paradigms. These findings establish a comprehensive framework for predicting ZrC performance across realistic service conditions and offer critical guidance for the design of ultra-high temperature carbides in extreme environments.

2. Materials and methods

2.1. Material fabrication

Zirconium carbide (ZrC) powder (purity: 99.5 %, particle size < 45 μm, Goodfellow, UK) was used as the starting material. The powder was placed into a 30 mm diameter graphite die inside a glovebox to minimize oxygen contamination, then transferred to a spark plasma sintering (SPS) furnace (FCT Systeme GmbH, Germany) and sintered under vacuum. A two-step sintering process was carried out: 1500 °C for 120 s followed by 2000 °C for 600 s under 80 MPa uniaxial pressure, with a heating rate of 3.3 °C/s. The initial 1500 °C hold was intended to minimize contamination prior to high-temperature sintering. After sintering, the sample was cooled to room temperature with a cooling rate of 0.4 °C/s and surface graphite was removed using a grinder-polisher (MetaServ 250, Buehler, USA). The resulting ZrC disk had a relative density of 98.7 ± 0.1 % calculated by the Archimedes method. The ZrC disk was polished with progressively finer grit papers, culminating in a mirror-like surface using a 1 μm polishing cloth. Lastly, the ceramic disk was machined into rectangular cuboids with dimensions $6 \times 6 \times 3$ mm^3 using a cutting machine (Secotom-60, Struers, Denmark) with a diamond cut-off wheel (M1D20). The precise carbon and oxygen contents of the sintered zirconium carbide were determined by elemental infrared analysis (EMIA) and elemental gas analysis (EMGA) (HORIBA, Japan), respectively. The reported values represent the average of three independent measurements. Based on the elemental analysis, the chemical composition of the sintered ceramic was $ZrC_{0.94}O_{0.05}$. The standard deviations of the carbon and oxygen measurements were 0.023 % and 0.016 %, respectively, indicating good measurement precision. The low oxygen content shows that oxygen incorporation was minimized during sintering process.

2.2. In-situ vacuum oxidation

The ZrC cuboids were heated from room temperature to the target temperatures (400, 600, 700, and 800 °C) at a heating rate of 0.2 °C/s under vacuum condition (5×10^{-2} Pa), where the reported pressure refers to the total chamber pressure. Each temperature was maintained isothermally for 10,800 s, during which in-situ X-ray diffraction (XRD) patterns were recorded at one-minute intervals. Following the isothermal dwell, the samples were cooled at an approximate rate of 0.2 °C/s in 50 °C increments, with XRD measurements acquired at each step prior to further cooling.

Thermal treatment was conducted in an Anton Paar XRK 900 chamber employing furnace-type resistive heating, controlled by an Anton Paar TCU 750 temperature control unit equipped with a Eurotherm 2604 PID controller. Vacuum condition was maintained at 5×10^{-2} Pa using an Adixen Drytel 1025 vacuum system (Pfeiffer Vacuum GmbH, Asslar, Germany), and continuously monitored using a Thyracont VSP64DL pressure transducer. The samples were mounted on a Si zero-diffraction wafer supported by a Macor holder within the reactor chamber.

The X-ray diffraction measurements were performed with a Bruker D8 Discover (Cu-Kα $\lambda = 0.1542$ nm, 40 kV, 40 mA). This diffractometer was equipped with a LYNXEYE XE detector operating in 1D high resolution mode and with an opening of 2.86 degrees (Bruker AXS GmbH, Karlsruhe, Germany). The XRD measurements were performed in Bragg-Brentano configuration with 2.0 mm fixed slit on the primary and secondary side. An additional 2.5 degree Soller slit was used on the primary side.

2.3. Ex-situ characterization

The microstructures and morphologies of the SPS-sintered zirconium carbide and corresponding oxide scale were analyzed via scanning electron microscopy (SEM) with a JSM-IT 100 (JEOL, Japan). Nanoscale characterization of the single-layer nanocrystalline oxide scale was performed using high-resolution transmission electron microscopy (HRTEM) with a double Cs-corrected JEM-ARM200F apparatus (JEOL, Japan) in conjunction with Energy-Dispersive X-ray Spectroscopy (EDX), employing a Dual SDD EDS system (JEOL, Japan). The lamella for HRTEM was prepared via Focused Ion Beam (FIB) (Helios G5 UC, Thermo Fisher Scientific, USA) with a Ga-focused ion beam. A protective platinum layer approximately 2–3 μm thick was first deposited on the region of interest via electron- and ion-assisted deposition. Coarse milling was performed using a 30 kV Ga^+ ion beam at high current (2.5–21 nA) to excavate trenches on either side of the lamella. The sample was then thinned to electron transparency using progressively lower ion beam currents (0.43 nA–1.1 pA). An in-situ NanoManipulator (EasyLift system) was used to lift out the lamella. Subsequently the lamella was mounted it onto a copper half-grid with ion-assisted Pt deposition.

3. Results and discussion

3.1. Single-layer nanocrystalline oxide scale formation

Under vacuum condition (5×10^{-2} Pa), SPS-sintered zirconium carbide develops a distinct single-layer composite scale during thermal exposure, as shown in Fig. 1(a). The scale exhibits a nanocrystalline structure, as evidenced by ring-like selected area electron diffraction patterns (SAEDP) (Fig. 1(c)). These rings display spotty and slightly elliptical diffraction features, indicating a distribution of fine grains accompanied by lattice distortion. Radial averaging of the diffraction rings obtained from high-resolution transmission electron microscopy (HRTEM) and SAED revealed d-spacings of approximately 2.97 Å, 2.54 Å, and 1.82 Å. These values correspond to the (111), (200), and (022) crystallographic planes of cubic zirconia (c-ZrO_{2-x}), confirming that the oxide scale adopts a cubic-dominant fluorite-like structure.

Notably, the SAEDP exhibit spotty and elongated diffraction features, particularly pronounced in the inner low-angle rings (Fig. 1(c)). The radial elongation of diffraction spots arises from lattice microstrain,

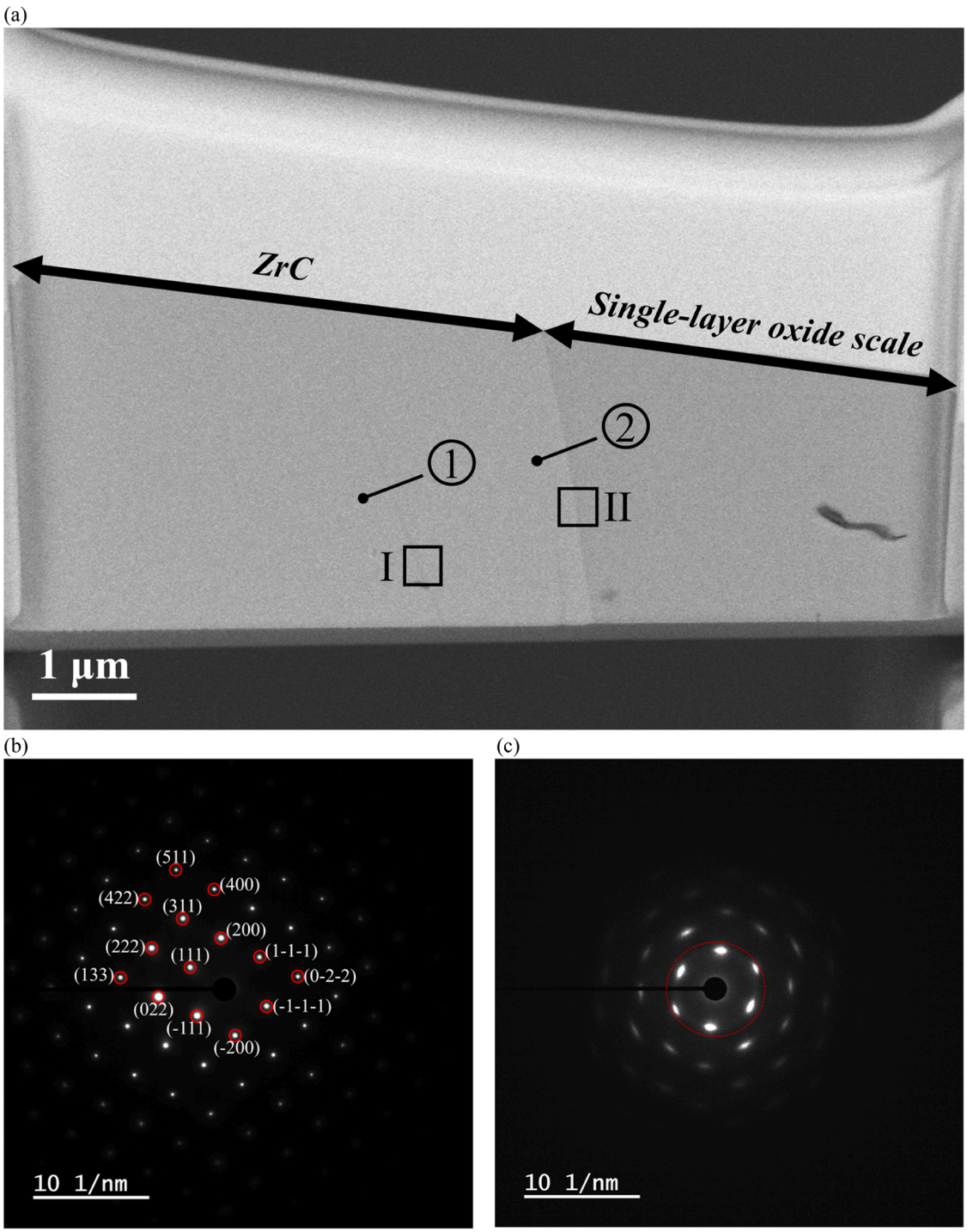


Fig. 1. Microstructural and crystallographic characterization of oxidized ZrC lamella. (a) Scanning electron microscopy (SEM) image of ZrC lamella after isothermal temperature 600 °C; under $< 5 \times 10^{-2}$ Pa; 10,800 s, followed by cooling to room temperature. A single-layer oxide scale is demonstrated in the image. Square I indicates the approximate region selected for the high-resolution transmission electron microscopy (HRTEM) analysis shown in Fig. 2 (oxidation front stripe), and Square II marks the indicative area presented in Fig. 3 (ZrC/single-layer scale interface). Line 1 denotes the position of the line scan corresponding to Fig. 4(a), and Line 2 indicates the location of the line scan shown in Fig. 4(b). (b) Selected area electron diffraction pattern (SAEDP) acquired from ZrC in (a) along [0 − 1 1] zone axis. The measured interplanar spacings (d_{hkl}) of approximately 2.72 Å (111), 2.36 Å (200), 1.66 Å (022), 1.42 Å (311), 1.18 Å (400), 0.96 Å (422), and 0.91 Å (511) are consistent with ZrC. (c) SAEDP of the single-layer oxide scale along the [0 − 1 1] zone axis. Radial averaging of the spotty diffraction rings yields d-spacings of approximately 2.97 Å, 2.54 Å, and 1.82 Å, indexed to the (111), (200), and (022) planes of cubic-ZrO_2 respectively. A broad diffuse halo (inside the red dashed circle) at a radial position corresponding to an average interatomic distance of ~3.4–3.6 Å indicates short-range ordering of amorphous carbon.

which produces a distribution of interplanar spacings and therefore broadening in the radial direction of reciprocal space. In contrast, tangential elongation reflects mosaicity, the small angular misorientations between neighboring nanocrystals, resulting in azimuthal smearing along the ring circumference. In addition to crystalline reflections, a broad diffuse halo is observed at a radial position corresponding to an average interatomic spacing of ~3.4–3.6 Å (dashed red circle in Fig. 1(c)). This feature is a characteristic of short-range ordering

in amorphous carbon. The absence of a discrete graphitic (002) reflection confirms the lack of long-range stacking order, indicating that the carbon phase remains structurally disordered rather than graphitized [24].

Collectively, these observations confirm the formation of a single-layer nanocrystalline cubic-dominant ZrO_2–amorphous carbon composite scale, in which microstrained ZrO_2 nanodomains are embedded within a disordered carbon matrix. This microstructure differs fundamentally from the double-layer scale reported under higher oxygen pressures [13,14,17,25,26]. In high oxygen pressure regime develops a double-layer structure: an inner Zr–C–O layer enriched in c-ZrO_2 and carbon, while the outer layer exhibits pronounced cracking and consists of a mixture of cubic/tetragonal and monoclinic ZrO_2 with significant carbon depletion [17].

The stark contrast between these scale morphologies can be rationalized thermodynamically. Under extremely oxygen-deficient conditions (e.g. $< 5 \times 10^{-2}$ Pa), the oxygen chemical potential is insufficient to fully oxidize carbon to gaseous CO/CO_2. According to the Ellingham diagram, Gibbs free energy for ZrO_2 formation is substantially more negative than that for carbon oxidation over a broad temperature range, indicating that zirconium preferentially oxidizes while carbon remains thermodynamically stable as a solid phase at oxygen-limiting conditions [27–29]. Consequently, a dense single-layer composite scale forms in which carbon is retained within the structure, without developing the double-layer morphology observed under higher oxygen pressures.

In contrast, at elevated oxygen pressures, the higher oxygen activity shifts the equilibrium within the oxide scale toward carbon oxidation ($C + O_2 \rightarrow CO_2$) once the local oxygen pressure reaches a critical threshold, which promotes the carbon depletion and evolution of gaseous products. The associated gas evolution and stress development contribute to through-thickness cracking in the outer oxide layer [13,18,30,31]. Simultaneously, the enhanced oxygen supply facilitates the formation of thicker zirconia scales with mixed cubic/tetragonal and monoclinic polymorphs [17]. Thus, tuning the oxygen pressure fundamentally alters the oxidation pathway from a dense strain-accommodating cubic-dominant ZrO_2–amorphous carbon nanocomposite under oxygen-limited conditions, to a double-layer, carbon-depleted, and mechanically compromised oxide scale under oxidizing atmospheres.

At the ZrC/nanocomposite scale interface after 10,800 s of isothermal exposure at 600 °C, oxidation front stripes were observed by HRTEM (Fig. 2(a)). The fast Fourier transform (FFT) pattern obtained from the oxidation front stripe (Fig. 2(c)) shows a broad diffuse halo corresponding to an average interatomic spacing of ~3.4–3.6 Å, indicative of short-range ordering consistent with amorphous carbon. This diffuse halo overlaps with spotty diffraction rings attributable to nanocrystalline c-ZrO_2, suggesting the coexistence of amorphous and crystalline oxidation products. Such stripe-like morphology at the ZrC/oxidized layer interface has also been reported under high oxygen partial pressures, where amorphous carbon and zirconia were found to coexist [17]. Squares III and V in Fig. 2(a) exhibit aligned lattice fringes, and their corresponding FFTs (Fig. 2(b)(d)) show cubic diffraction patterns consistent with crystalline ZrC. The identical crystallographic orientations suggest that both regions (Squares III and V in Fig. 2(a)) may originate from a common parent ZrC grain that has been partially modified by an oxidation front. Further discussion of the oxidation front features at the carbide–oxide scale interface, which are also captured by SEM, is presented in Section 3.3.1. For the single-layer scale, HRTEM characterization was also performed near the ZrC/scale interface, along with corresponding FFT analysis (Fig. 3). The FFT pattern shown in Fig. 3(c) exhibits a pronounced diffuse halo with an average interatomic spacing of 3.4–3.6 Å, again signifying short-range order typical of amorphous carbon. This observation is consistent with the SAED pattern in Fig. 1(c), which also displays a diffuse halo.

In addition to structural characterization, compositional profiling across the oxidation fronts was conducted using HRTEM–EDX (Fig. 4). A distinct compositional transition zone was identified, indicating the probable formation of a zirconium oxycarbide phase, reflecting progressive oxygen incorporation into the zirconium carbide lattice. The purple dashed square regions in Fig. 4(a)(b) delineate these transition zones, where the oxygen atomic percentage increases from its initial rise to near saturation. These regions correspond to the oxidation front stripes and the carbide/oxide interface, which have likewise been reported for ZrC oxidized under elevated oxygen partial pressures. Previous studies under high oxygen pressures identified nanometer-scale proximal zones of 20–30 nm region adjacent to the Zr–C–O inner layer [17]. In contrast, under vacuum thermal exposure, the probable oxycarbide region formed is substantially thicker, more than twice that was reported under 2 %O_2–98 %Ar at the same temperature. Specifically, a 70–80 nm proximal zone adjacent to the single-layer scale (purple dashed region in Fig. 4(b)) is observed. Although HRTEM–EDX is not sufficiently sensitive to reliably quantify very low oxygen concentrations within ZrC, the observed HRTEM–EDX profile nevertheless reveals a clear compositional gradient accompanied by pronounced thickening under oxygen-limited condition. This likely indicates the promotion of progressive formation of a zirconium oxycarbide phase rather than a sharp oxide interface. Consequently, the broadened compositional transition zone observed in the HRTEM–EDX map is plausibly indicative of a diffuse oxycarbide zone, characterized by a continuous variation in composition rather than a well-defined phase boundary.

3.2. Isothermal ZrC behavior and nanocrystalline oxide growth

In-situ XRD measurements were performed under isothermal conditions at 400 °C to monitor the structural evolution of ZrC during thermal exposure. The short-scan isothermal monitoring of the ZrC (111) reflection (Fig. 5(a)) shows that the peak intensity decreases from 67.8 at the beginning of the exposure to 50.5 after 5400 s, followed by a partial recovery to 60.8 at 10,800 s. This non-monotonic evolution suggests an initial redistribution of crystallographic orientations or lattice perturbation, followed by partial structural stabilization. More detailed insight is provided by the full-scan patterns (Fig. 5(b)). The intensities of ZrC peaks evolve as follows: (111) decreases from 68.6 to 61.1, (200) from 62.9 to 59.2, (220) from 58.5 to 39.6, (311) from 42.1 to 36.4, and (222) from 18.4 to 13.4. Notably, the (220) reflection exhibits the most pronounced reduction in intensity, decreasing by nearly one-third relative to its initial value. The disproportionate reduction of the (220) peak may indicate reorientation of grains associated with this crystallographic plane. Consequently, the in-situ XRD results demonstrate that even at 400 °C under isothermal conditions, ZrC undergoes measurable crystallographic redistribution and orientation-dependent structural evolution. This behavior may likely be driven by interfacial reactions, accompanied by minor oxygen incorporation into the lattice, leading to the formation of a low-oxygen-content oxycarbide phase at the surface [32].

At 600 °C, isothermal in-situ XRD analysis reveals clear evidence of progressive surface oxidation. Specifically, the emergence of a very broad diffraction peak at $2\theta = 30.42^{\circ}$, corresponding to the (111) reflection of c-ZrO_2, indicates the formation of nanocrystalline cubic-dominant zirconia. The pronounced peak broadening suggests a nanoscale grain size and/or significant lattice strain within the newly formed oxide. The short-scan monitoring of the ZrC (111) reflection (Fig. 6(a)) shows a continuous and substantial decrease in intensity from 19.3 ultimately to 3.5. This sharp reduction confirms that the surface concentration of ZrC progressively diminishes during isothermal exposure, consistent with its consumption through oxidation. This trend is further corroborated by the full-scan data (Fig. 6(b)), with the intensities of ZrC reflections decreasing dramatically. The near-uniform and severe reduction across all major diffraction planes indicates that ZrC is being extensively consumed at the surface rather than undergoing simple texture evolution. Concurrently, multiple broad peaks characteristic of c-ZrO_2 become increasingly pronounced. The breadth of these peaks

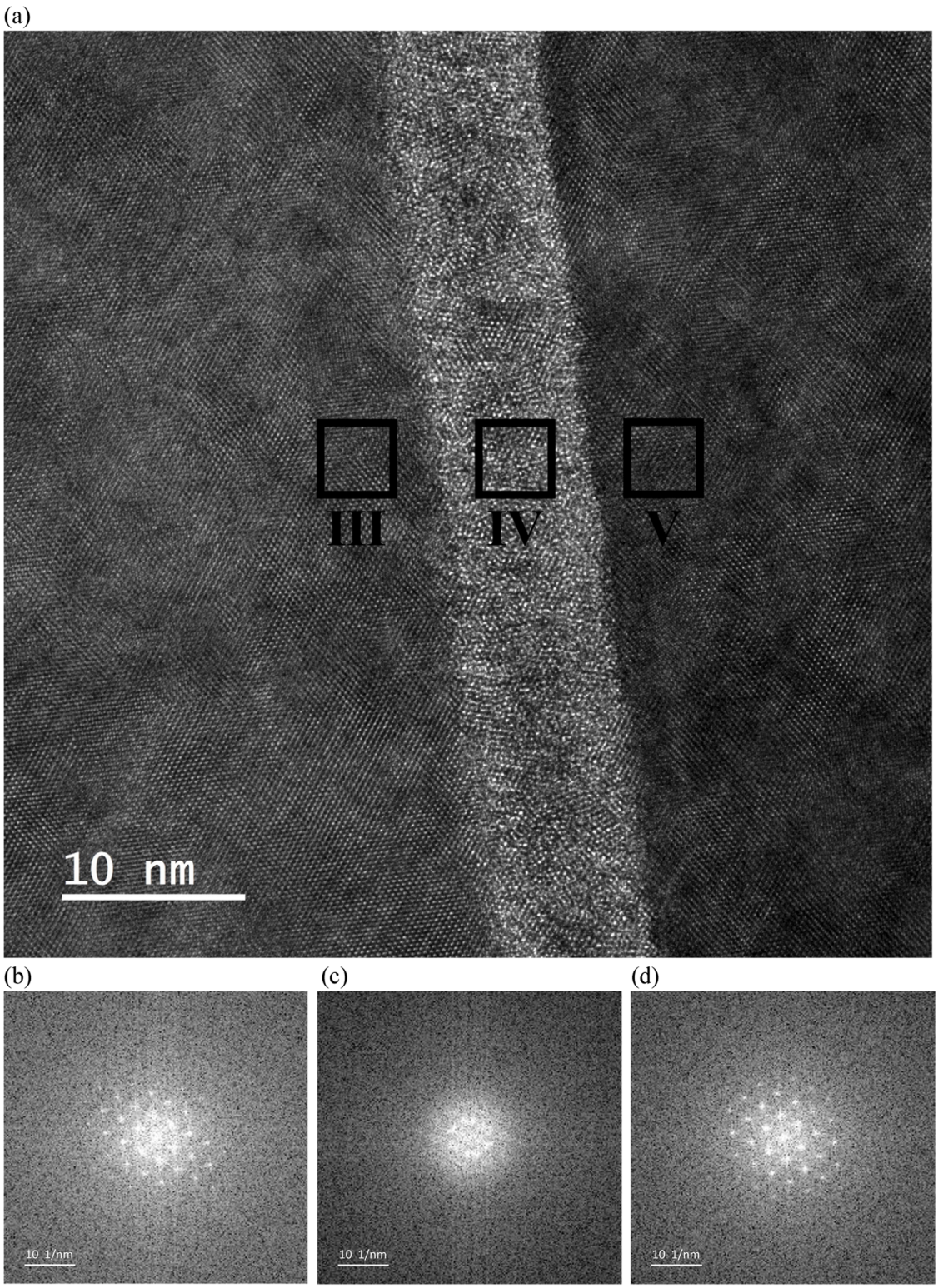


Fig. 2. Atomic-scale characterization of the oxidation front in ZrC. (a) HRTEM image acquired along the [0 − 1 1] zone axis at the oxidation front stripe. The magnified view of the oxidation front stripe appears as the central bright contrast region. The image was collected from Square I in Fig. 1(a). (b) Fast Fourier transform (FFT) pattern obtained from Square III in (a), exhibiting cubic diffraction spots characteristic of the crystalline ZrC. (c) FFT pattern from the oxidation front stripe (Square IV in (a)), displaying a broad diffuse halo corresponding to an average interatomic spacing of ~3.4–3.6 Å, indicative of short-range ordering consistent with amorphous carbon. The diffuse halo overlaps with spotty diffraction rings attributable to nanocrystalline ZrO_2, suggesting the coexistence of amorphous and crystalline oxidation products. (d) FFT pattern from Square V in (a), confirming the cubic ZrC structure.

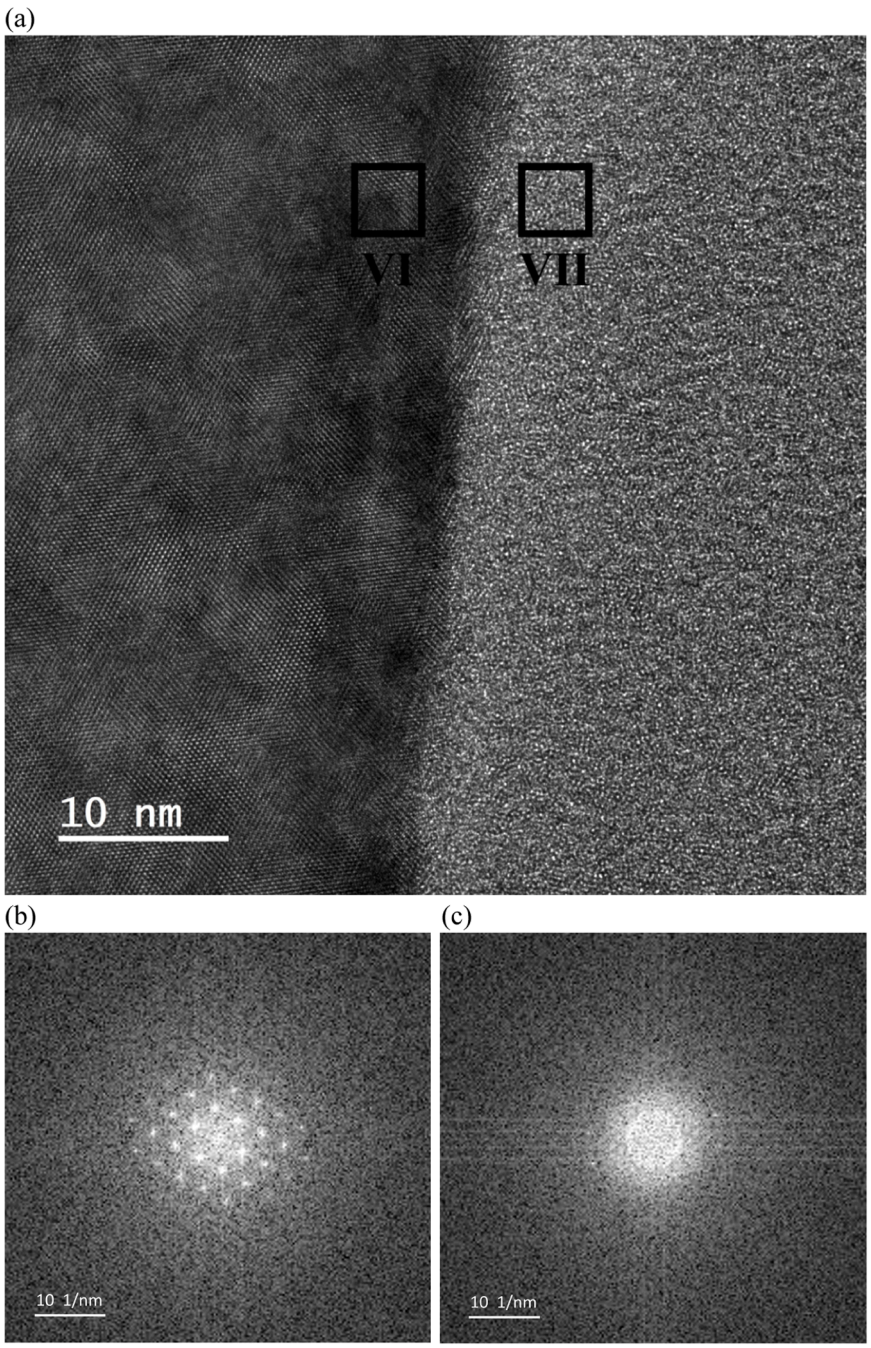


Fig. 3. Atomic-scale structure of the ZrC/single-layer scale interface. (a) HRTEM image acquired along the [0 − 1 1] zone axis at the interface between ZrC (left) and the single-layer oxide scale (right). The image was obtained from Square II in Fig. 1(a), highlighting the structural transition across the interface. (b) FFT pattern from Square VI in (a), exhibiting cubic diffraction spots characteristic of the ZrC. (c) FFT pattern from the single-layer scale region (Square VII in (a)) adjacent to the interface, exhibiting a diffuse halo with an average interatomic spacing 3.4–3.6 Å, signifying the presence of short-range order typical of amorphous carbon.

confirms the formation of nanocrystalline zirconia rather than well-developed bulk oxide.

Further increasing the temperature to 700 °C during the in-situ isothermal measurements resulted in a faster growth of c-ZrO_2. In the short scan (Figure S1 (a)), the ZrC (111) peak intensity decreased markedly from 3.8 to nearly zero. In contrast, the c-ZrO_2 peaks increased significantly in intensity. In comparison with 600 °C, the (200) reflection of c-ZrO_2 becomes clearly visible at 700 °C, whereas it was subtle at 600 °C. This indicates that ZrC diminishes while c-ZrO_2 grows more progressively. The full scan results (Figure S1 (b)) further confirm this transformation, with ZrC peak intensities decreasing substantially with increasing temperature. Meanwhile, c-ZrO_2 diffraction peaks show a clear rise in intensity. These results demonstrate enhanced crystallization and growth of cubic-dominant ZrO_2 at 700 °C, as evidenced by the emergence and strengthening of the 35.27° (200) diffraction peak.

Lastly at 800 °C, the in-situ isothermal XRD patterns reveal further phase evolution. The short scan (Fig. 7(a)) shows the continued development of diffraction peaks corresponding to c-ZrO_2 at $2\theta = 30.42°$ (111) and 35.27° (200). The extended 2θ scan (Fig. 7(b)) confirms the dominance of c-ZrO_2 and additionally reveals the emergence of tetragonal-like ordering of ZrO_2, evidenced by the (202) reflection at $2\theta = 62.68°$. No diffraction peaks associated with ZrC are detected at this temperature, indicating complete consumption of the ZrC phase at the surface. These observations show that at 800 °C, the surface is fully

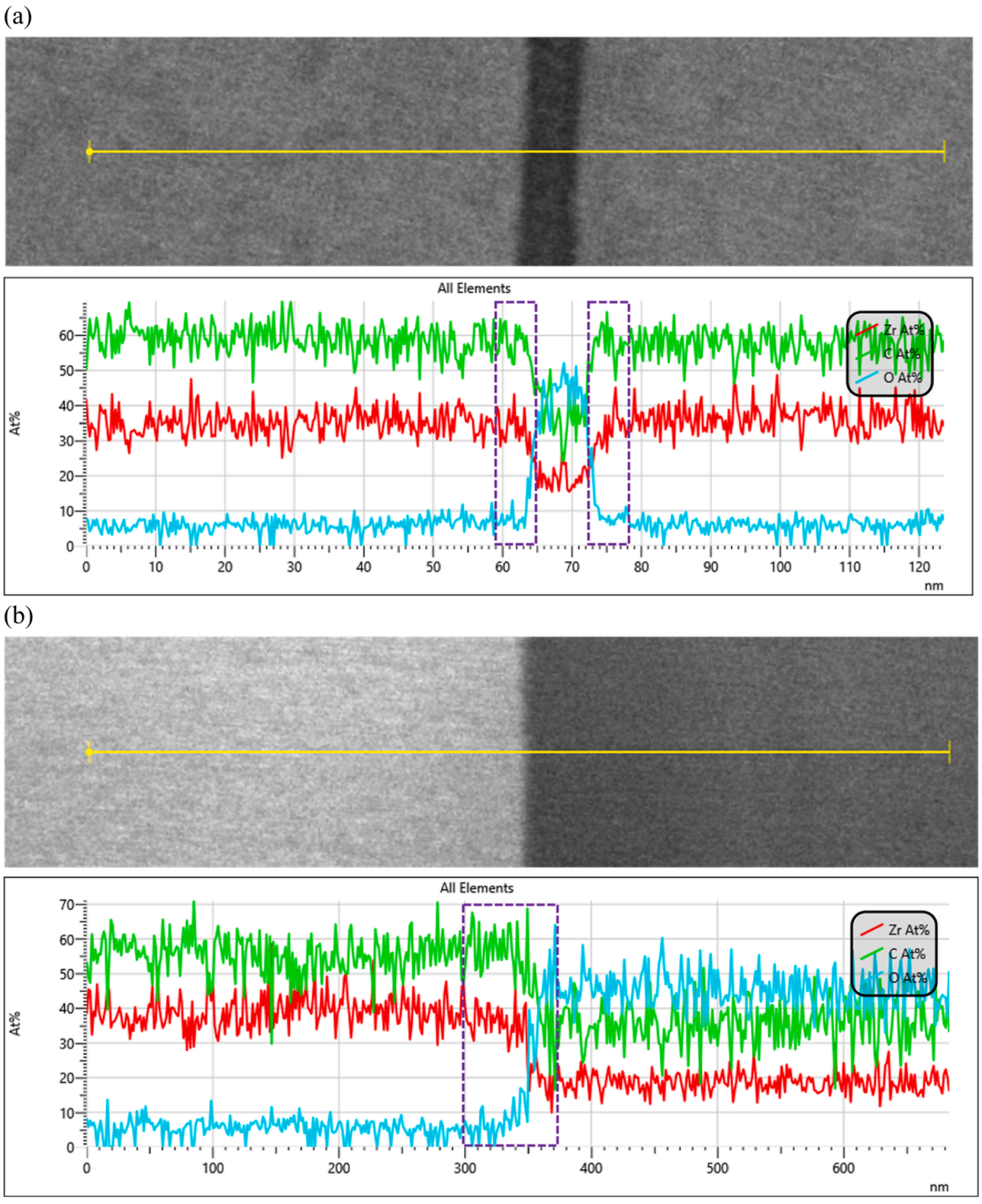


Fig. 4. Compositional profiling across the oxidation front by HRTEM–EDX. (a) HRTEM–EDX line scan acquired along Line 1 in Fig. 1(a), showing the spatial variation of elemental concentrations across the oxidation front stripe. (b) HRTEM–EDX line scan along Line 2 in Fig. 1(a). The purple dashed square regions in (a)(b) delineate the compositional transition zone from the onset of increasing O at% to a plateau where O at% stabilizes with minimal variation. This transitional region is indicative of the probable formation of a zirconium oxycarbide phase, reflecting progressive oxygen incorporation into the zirconium carbide lattice.

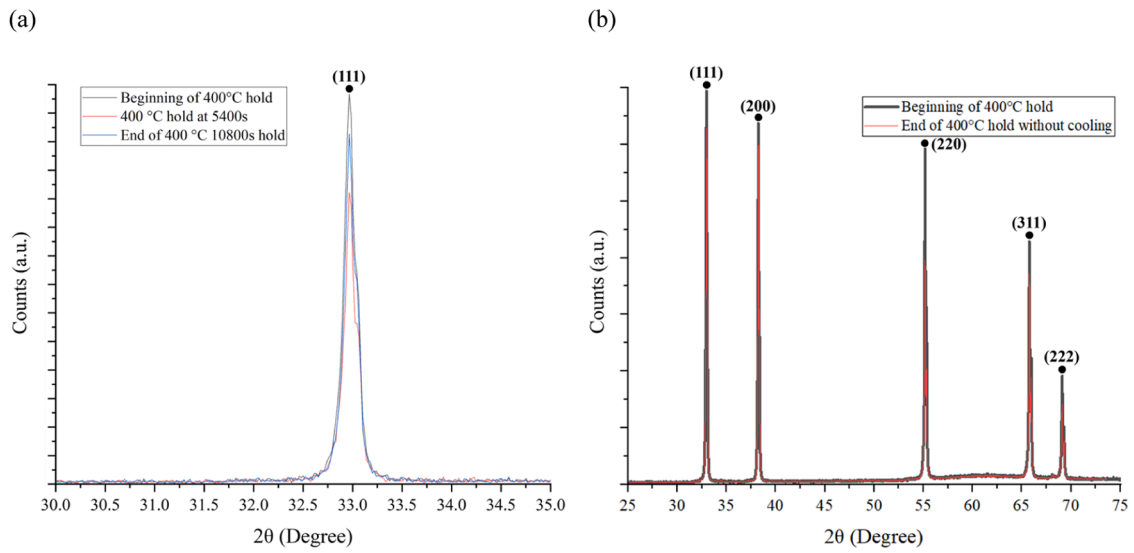


Fig. 5. In-situ XRD analysis at 400 °C. (a) XRD patterns highlighting the evolution of the (111) crystallographic plane of ZrC. (b) Extended 2θ scans collected under isothermal exposure. ●: ZrC.

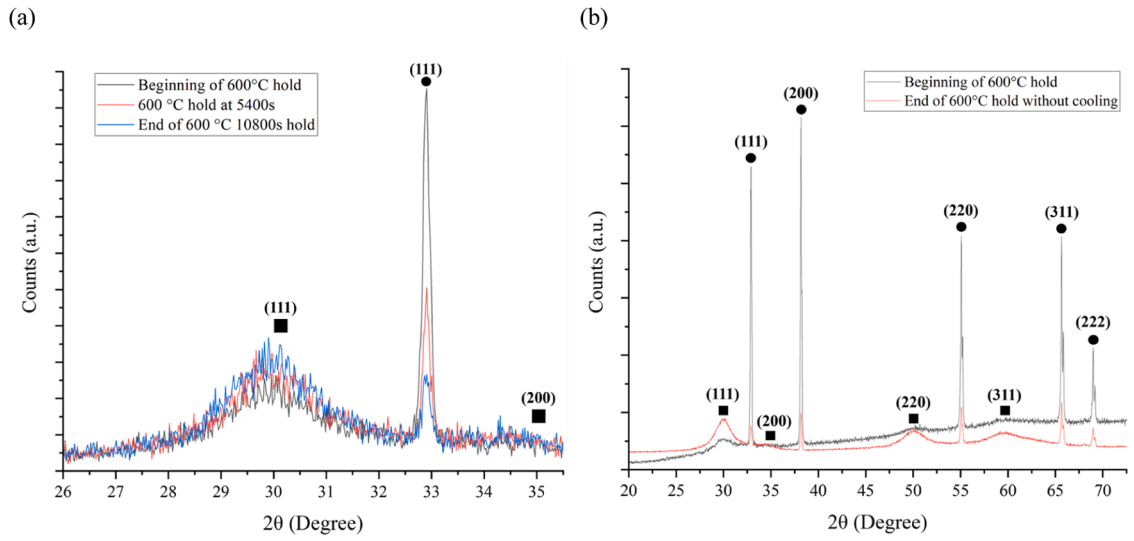


Fig. 6. In-situ XRD analysis at 600 °C. (a) XRD patterns showing the evolution of broad diffraction features of c-ZrO_2 at 2θ = 30.42° (111) and 35.27° (200), together with a sharp reflection corresponding to (111) plane of ZrC. (b) Extended 2θ scan recorded during isothermal exposure. ●: ZrC ■: c-ZrO_2.

oxidized with coexistence of cubic and tetragonal ZrO_2 polymorphs. The appearance of the tetragonal phase suggests enhanced oxidation kinetics and reflects the formation of a larger crystalline oxide.

3.3. ZrC and nanocrystalline oxide evolution upon cooling

3.3.1. ZrC behavior and ZrO2 size- and temperature-controlled phase stability

In addition to the isothermal in-situ analysis, in-situ XRD measurements were also performed during cooling from the isothermal exposure temperature down to room temperature. For the sample exposed at 400 °C, the diffraction peak intensities of ZrC remained similar during cooling to room temperature (Figure S2). No significant variation in peak position or intensity was detected. These results indicate that the crystallographic texture and phase constitution of ZrC remain stable during cooling, with no detectable phase transformation or microstructural evolution occurring in this temperature range. This suggests that carbide maintains its structural stability after long-duration low-temperature thermal exposure, without the formation of a coherent oxide scale, as evidenced in Fig. 8(b). However, a weak and very broad diffraction feature is detected in the XRD pattern within the 2θ range of 55–65°, indicating the possible formation of an amorphous phase (Fig. 8 (a)). This broad peak may be associated with a small amount of amorphous oxide or disordered carbon species localized at the near-surface region, although no distinct crystalline oxide peaks are observed.

For the sample cooled from 600 °C, the short-scan XRD results of ZrC (Figure S3) indicate a slight decrease in the intensity of the (111) diffraction peak. In the full XRD scan, the ZrC patterns (Fig. 9(a)), particularly at higher angles, exhibit a more pronounced decrease in peak intensities upon cooling. The cubic-dominant fluorite-like phase remained stable during cooling from 600 °C to room temperature, as demonstrated in Figure S3 and Fig. 9(a). From microstructural SEM examination (Fig. 9(b)) after isothermal exposure for 10,800 s at 600 °C followed by cooling to room temperature, we observed that the oxide layer appears as a single dense 13.45 ± 0.74 μm thick layer without through-thickness cracks and with only minimal in-plane cracking. This behavior contrasts markedly with oxide scales formed under higher oxygen pressures. Previous studies conducted in 2–21 % O_2

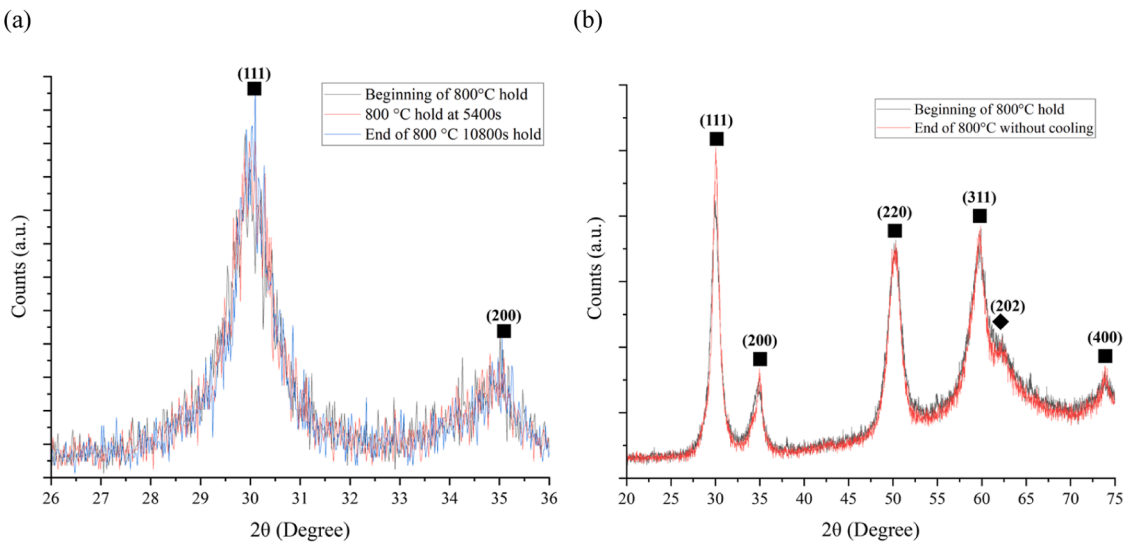


Fig. 7. In-situ XRD analysis at 800 °C. (a) XRD patterns showing the evolution of broad diffraction features of c-ZrO_2 at 2θ = 30.42° (111) and 35.27° (200). (b) Extended 2θ scan recorded during isothermal exposure. ■: c-ZrO_2 ◆: t-ZrO_2.

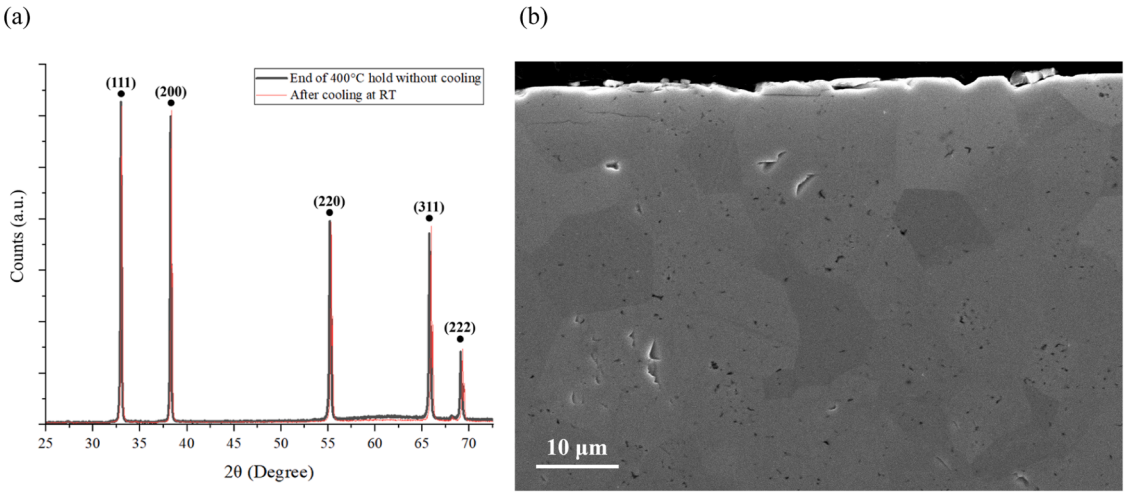


Fig. 8. In-situ XRD analysis during cooling from 400 °C. (a) Extended 2θ scans collected before and after cooling to room temperature. ●: ZrC (b) Cross-sectional SEM image of the sample after cooling from 400 °C to room temperature, showing no coherent oxide scale formation.

environments under the same isothermal oxidation duration (10,800 s) and temperature (600 °C) reported significant through-thickness cracking within the oxide scale [17,18]. In addition, the dense monolayer oxide scale before through-thickness cracking is merely 3.85 ± 0.49 μm under oxygen-rich conditions [17], which is substantially thinner than the thickness observed under constrained oxygen environment. These observations suggest that limiting the oxygen supply delays crack initiation while enabling the development of a thicker structurally stable oxide layer. Notably, the SEM image in Fig. 9(b), highlighted by the red box, reveals the carbide–oxide scale interface. Consistent with our HRTEM observations presented in Figs. 1 and 2, the SEM analysis also identifies stripe-like oxidation fronts at the interface, further corroborating the characteristic interfacial oxidation morphology. These observations suggest that oxidation propagates non-uniformly within the ZrC grains and throughout the carbide matrix. Although the origin of the stripe-like oxide penetrations remains unresolved, the available experimental evidence suggests that they arise from orientation-dependent oxide nucleation coupled with stress-assisted interface evolution.

TEM studies have demonstrated that c-ZrO_2 nucleates on the ZrC lattice with well-defined crystallographic orientation relationships, indicating that oxide formation is crystallographically constrained rather than random [31,33]. Such orientation-dependent nucleation may favor localized advancement of the oxidation front within individual ZrC grains, leading to discrete oxide penetrations rather than a uniformly migrating interface. Furthermore, DFT calculations suggest that oxygen incorporation into ZrC is crystallographically dependent, with the (100) and (111) surfaces exhibiting more favorable oxygen adsorption and incorporation energetics than other low-index surfaces [34,35].

Following the initial oxide formation, the ZrC-to-ZrO_2 transformation is accompanied by volume expansion, carbon rejection, and CO/CO_2 evolution, all of which are expected to generate localized stresses at the reaction front [14,30]. These stresses may destabilize an otherwise planar oxidation interface, while the associated defects may further facilitate localized oxygen transport, thereby sustaining oxide growth along the initially oxidized regions, and promoting the observed stripe morphology.

Overall, in this study, the combined phase stability and crack-resistant microstructure of the scale demonstrate that oxidation at

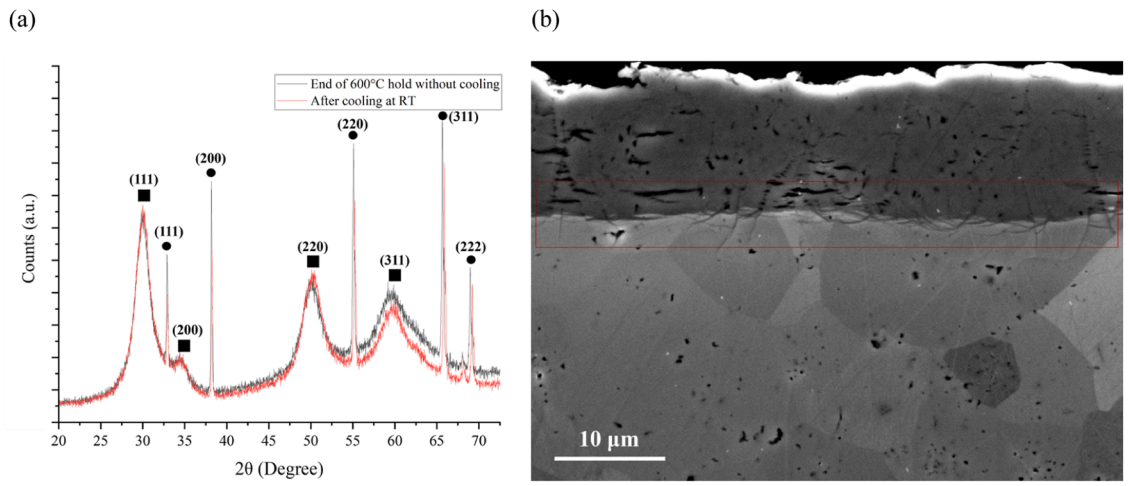


Fig. 9. In-situ XRD analysis during cooling from 600 °C. (a) Extended 2θ scans collected before and after cooling to room temperature. ●: ZrC ■: c-ZrO_2 (b) Cross-sectional SEM image of the sample after cooling from 600 °C to room temperature. The red box highlights the carbide–oxide interface and the associated oxidation fronts.

600 °C under oxygen-scarce conditions promotes the formation of a structurally stable oxide scale, distinguishing it from scales formed under high oxygen pressures.

While ZrC cooled from isothermal 700 °C after 10,800 s, the phase constitution remains comparable to that observed at 600 °C, with c-ZrO_2 remaining dominant during cooling, as indicated in Figure S4 and Fig. 10(a). However, a notable difference is observed in the relative peak intensities. In the 700 °C sample, the c-ZrO_2 diffraction peaks exhibit higher intensities compared to the 600 °C condition, indicating a thicker oxide scale and improved crystallinity of the oxide layer formed at the higher temperature. In contrast, the ZrC reflections are substantially diminished relative to the 600 °C sample. Only weak residual ZrC peaks are detectable at $2\theta = 55.12°$, 65.71°, and 69.03°, while the lower-angle reflections are absent. This pronounced reduction of ZrC peaks suggests extensive oxidation and a much greater consumption of the carbide at 700 °C. SEM micrographs (Fig. 10(b)) further corroborate the XRD results. The oxide scale formed at 700 °C after 10,800 s of isothermal exposure appears as a single-layer structure with a thickness of 33.85 ± 0.85 μm. Compared to the 600 °C scale, however, the 700 °C oxide exhibits significantly more pronounced in-plane cracking. These cracks are likely associated with enhanced oxide growth stresses and the increased crystallite size of c-ZrO_2 formed at higher temperature, consistent with crystallite sizes extracted from the Williamson–Hall analysis of the zirconia nanocrystals (discussed in the following section). Importantly, despite the presence of substantial in-plane cracks, no through-thickness cracks are observed. From the Ellingham diagram, under oxygen-limited conditions ($< 5 \times 10^{-2}$ Pa), carbon remains stable as a solid phase. Consequently, extensive CO/CO_2 gas evolution is suppressed, preventing internal gas-pressure buildup that would otherwise promote through-thickness cracking. As a result, the oxide scale maintains a single-layer morphology without penetrating cracks. This behavior contrasts sharply with oxide scales formed at the same temperature (700 °C) and exposure duration (10,800 s) under high oxygen pressures, exhibiting a double-layer oxide structure characterized by extensive through-thickness and in-plane cracking along with significant carbon depletion in the outer scale region [18]. Additionally, in an oxygen-rich environment at 700 °C, the dense monolayer oxide reaches a thickness of 15.05 ± 0.93 μm prior to the onset of through-thickness cracking [17]. This value is approximately half that of the single-layer oxide formed under oxygen-deficient condition. While oxidation at 700 °C leads to thicker oxide formation and greater ZrC consumption compared to 600 °C, the oxygen-limited environment enables the formation of a single-layer, adherent oxide scale without catastrophic through-thickness cracking, demonstrating improved structural stability

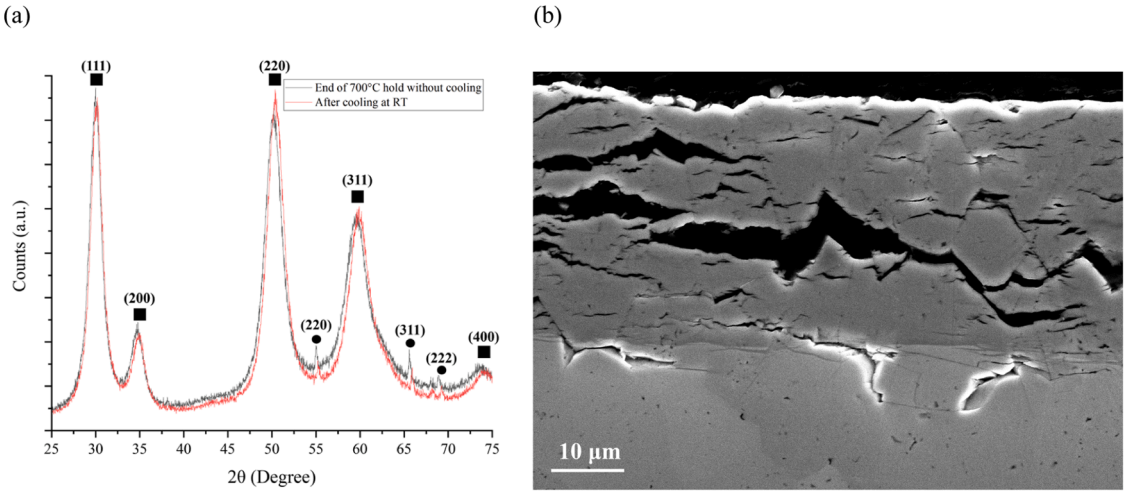


Fig. 10. In-situ XRD analysis during cooling from 700 °C. (a) Extended 2θ scans collected before and after cooling to room temperature. ●: ZrC ■: c-ZrO_2 (b) Cross-sectional SEM image of the sample after cooling from 700 °C to room temperature.

compared to high oxygen pressure conditions.

When isothermal temperature increases to 800 °C, the short in-situ XRD scans provide clear insight into the temperature-dependent phase evolution of zirconia. From 800 °C down to 450 °C (Figure S5 (a)), zirconia remains stable, without monoclinic phase detected. However, upon further cooling from 450 °C to 350 °C (Fig. 11(a)), the onset of phase transformation to the monoclinic phase becomes evident. Weak but observable monoclinic ZrO_2 (m-ZrO_2) peaks emerge at $2\theta = 28.10°$ (11–1) and 31.47° (111). From ~350 °C down to room temperature (Figure S5 (b)), the transformation becomes pronounced. Strong m-ZrO_2 reflections appear at $2\theta = 28.10°$ (11–1) and 31.47° (111), clearly indicating that the oxide phase progressively transforms into the thermodynamically stable monoclinic phase upon cooling. Fig. 11(c) illustrates the evolution of the XRD peak intensity corresponding to the (11–1) plane of m-ZrO_2 during in-situ cooling from 800 °C to ambient temperature. These observations suggest that the transformation into the monoclinic phase is temperature-dependent, occurring during cooling at approximately 400 °C, and not at isothermal temperatures, with crystallite growth likely playing a governing role. As the crystal size increases during high-temperature exposure, the stabilization effect associated with nanoscale zirconia diminishes, enabling the phase transformation upon cooling. A quantitative discussion of zirconia crystallite size, based on the Williamson-Hall method, will be presented in the following section. The long scan (Fig. 11(b)) further strengthens this interpretation. During isothermal exposure at 800 °C for 10,800 s, no obvious evidence of transformation to the monoclinic phase is observed. The oxide includes cubic zirconia, and the emergence of t-ZrO_2 (202) reflection at $2\theta = 62.68°$. This indicates that tetragonal component developments as crystallite growth proceeds.

In contrast, after cooling to lower temperatures, distinct m-ZrO_2 peaks emerge at $2\theta = 24.01°$ (011), 28.10° (11–1), and 31.47° (111). The appearance and progressive intensification of these reflections clearly demonstrate that the monoclinic phase transformation occurs during cooling rather than at high temperature. The transformation temperature of the vacuum-grown scale in the present study (~ 400 °C) is substantially lower than coarse-grained undoped zirconia, with the tetragonal-to-monoclinic transformation during cooling reported to occur at 950–1050 °C [36,37]. This marked deviation is attributed to the microstructural characteristics of the vacuum-grown oxide scale. HRTEM analysis reveals a nanocrystalline ZrO_2–C composite layer, while the SAED patterns exhibit spotty and radially elongated diffraction features, particularly in the low-angle rings indicative of microstrain (Fig. 1(c)). The combined effects of nanoscale crystallite dimensions, high defect density, interfacial constraints and strain energy are known to modify the relative stability of tetragonal and monoclinic zirconia, enabling t-ZrO_2 to persist far outside its equilibrium stability regime [38–41].

An additional noteworthy observation arises from the SEM

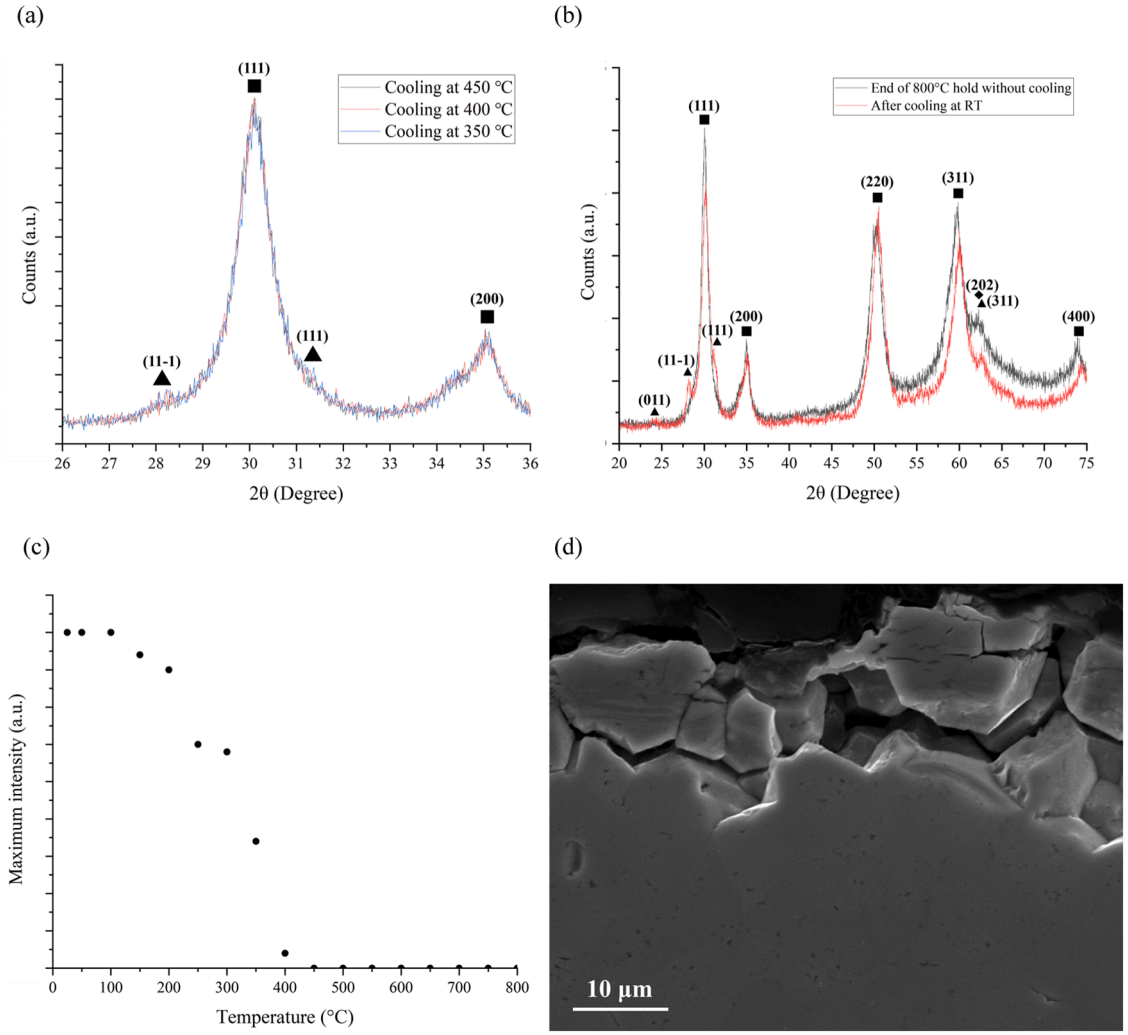


Fig. 11. In-situ XRD analysis during cooling from 800 °C. (a) XRD patterns collected during cooling from 450 °C to 350 °C. (b) Extended 2θ scans collected before and after cooling to room temperature. ■: c-ZrO_2 ◆: t-ZrO_2 ▲: m-ZrO_2 (c) Maximum XRD peak intensity evolution of m-ZrO_2 (11–1) plane at $2\theta = 28.10°$ during in-situ cooling from 800 °C to room temperature. (d) Cross-sectional SEM image of the sample after cooling from 800 °C to room temperature.

micrographs (Fig. 11(d)). Instead of forming a coherent oxide scale, pronounced cracks are observed along the ZrC grain boundaries after isothermal oxidation at 800 °C. This microstructural feature indicates that oxidation is not governed solely by lattice diffusion but is also strongly influenced by enhanced grain boundary diffusion. Such behavior aligns with the previously reported kinetic study [18], in which enhanced grain boundary diffusion was observed in SPS-sintered ZrC at temperatures of 800 °C and above. From the Arrhenius analysis, a clear turning point was revealed at 800 °C across oxygen pressures ranging from 2 % to 21 % O_2 [18], indicating a transition in the dominant diffusion mechanism. The present observations under oxygen-limited vacuum condition independently confirm this critical temperature. Taken together, the XRD results, SEM observations, and prior kinetic analyses identify 800 °C as a mechanistic transition threshold, above which oxidation shifts into an enhanced grain boundary diffusion regime. A comparative summary of all the full scan XRD patterns is presented in Figure S6, where the diffraction profiles obtained after isothermal oxidation at different temperatures are stacked to illustrate the phase evolution before and after cooling to room temperature.

To estimate the crystallite size of the zirconia nanocrystals, the Williamson–Hall method (Fig. 12) was employed. In this approach, the product of the full width at half maximum (FWHM) and $\cos\theta_{hkl}$ is plotted along the y-axis against $\sin\theta_{hkl}$ on the x-axis, enabling separation of size- and strain-induced broadening contributions. The relationship is expressed in Eq. (1):

$$(FWHM)(\cos\theta_{hkl}) = 4\varepsilon\sin\theta_{hkl} + \frac{K\lambda}{L} \quad (1)$$

where FWHM is the full width at half maximum of the diffraction peak in radians, θ_{hkl} is the Bragg angle, ε is the microstrain, K is the shape factor, λ is the X-ray wavelength (nm), and L is the crystallite size (nm). In this study, a shape factor of K = 1 was adopted. The microstrain ε was obtained from the slope of the linear fit, while the y-intercept provides the crystallite size L. For the purpose of peak fitting and Williamson–Hall analysis, the cubic-dominant fluorite-like ZrO_2 nanostructure was approximated as a c-ZrO_2 phase due to peak broadening and peak overlap arising from nanocrystallinity and lattice microstrain, which prevent reliable resolution of cubic and tetragonal contributions.

The results reveal a pronounced temperature dependence of both parameters, as well as the effect of cooling. At 600 °C, the crystallite size remains similar in the nanometer regime, with L ≈ 12 nm during isothermal exposure and after cooling to room temperature. The corresponding microstrain is approximately 2 % in both isothermal and after cooling to room temperature. At 700 °C, moderate grain growth is observed, with L increasing from 14 nm (isothermal) to 16 nm after cooling. The ε is around 1 % under isothermal condition and remains nearly constant upon cooling. In contrast, at 800 °C substantial coarsening occurs, with L reaching 81 nm during isothermal exposure. However, after cooling, the c-ZrO_2 crystallite size decreases to 57 nm, with ε about 1 % in both isothermal and cooled conditions. The reduction in c-ZrO_2 crystallite size is ascribed to the progressive phase transformation of larger cubic crystallites, ultimately culminating in the formation of the monoclinic phase upon cooling, as corroborated by in-situ XRD results (Fig. 11(c)).

The microstrain at 600 °C, approximately 2 %, is relatively high but remains physically reasonable for oxide nanoparticles in the 10–15 nm size range. Such elevated strain levels can be attributed to intrinsic nanoscale effects, including strong surface stress, and high concentration of oxygen vacancies. These structural heterogeneities generate non-uniform lattice distortions that manifest as peak broadening in the diffraction patterns (Figs. 6 and 9). In addition, extrinsic constraints imposed by the surrounding amorphous carbon matrix may contribute to the apparent strain. Interfacial mismatch and mechanical confinement can enhance lattice distortion and further broaden diffraction peaks, thereby amplifying the strain estimated by Williamson–Hall analysis.

3.3.2. *Oxygen pressure influence on oxide scale formation*

In our previous work, we investigated the oxidation of ZrC under higher oxygen partial pressure (2 % O_2) [17]. In comparison to our current results, we observe that, for all isothermal oxidation temperatures, the XRD peaks of the vacuum-treated samples are broader upon cooling to room temperature (Fig. 13(a)(b)(c)), indicating the presence of nanocrystalline domains. At 600 °C, no phase transformation occurs in either vacuum-grown or 2 % O_2-grown samples (Fig. 13(a)). However, at 700 °C, the m-ZrO_2 phase begins to appear (Fig. 13(b)), suggesting that crystallite size plays a critical role. Larger crystals, formed under higher oxygen pressure, transform to the monoclinic phase upon cooling. This behavior is even more pronounced at 800 °C under high oxygen pressure. The XRD pattern (Fig. 13(c)) shows very sharp and well-defined monoclinic peaks. For 800 °C, the characteristic (c-ZrO_2) peak at 2θ = 30.42° (111) shows a significant drop in normalized intensity from 0.91 in vacuum-grown sample to 0.08 under high oxygen pressure. m-ZrO_2 reflections dominate, while in vacuum-grown oxides show mostly cubic/tetragonal phases with only some monoclinic content. This confirms that besides temperature, the crystallite size of thermally grown zirconia from carbide is a critical factor that

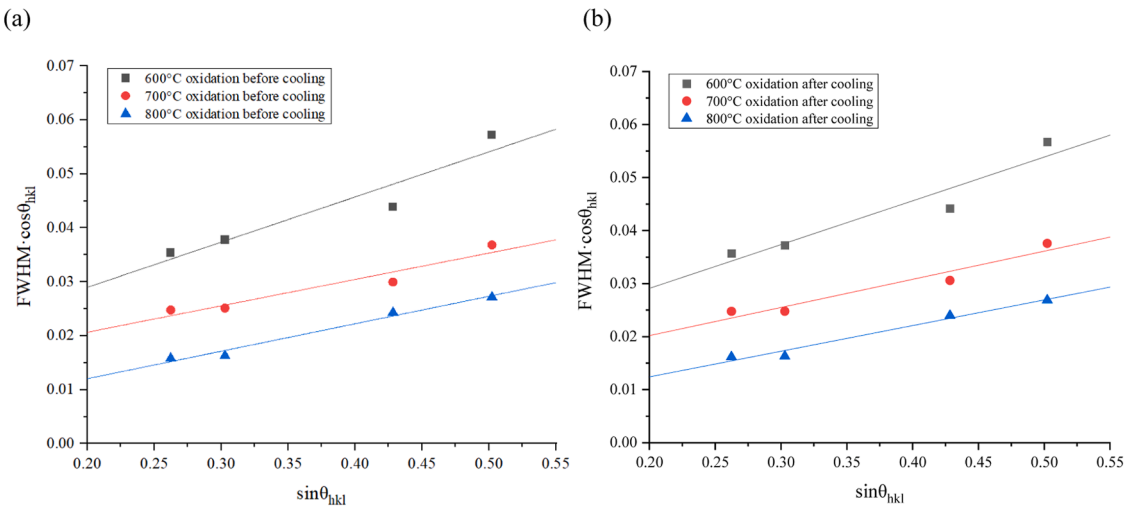


Fig. 12. Williamson–Hall analysis of thermally grown c-ZrO_2. (a) Williamson–Hall plot for c-ZrO_2 before cooling. (b) Williamson–Hall plot after cooling to room temperature.

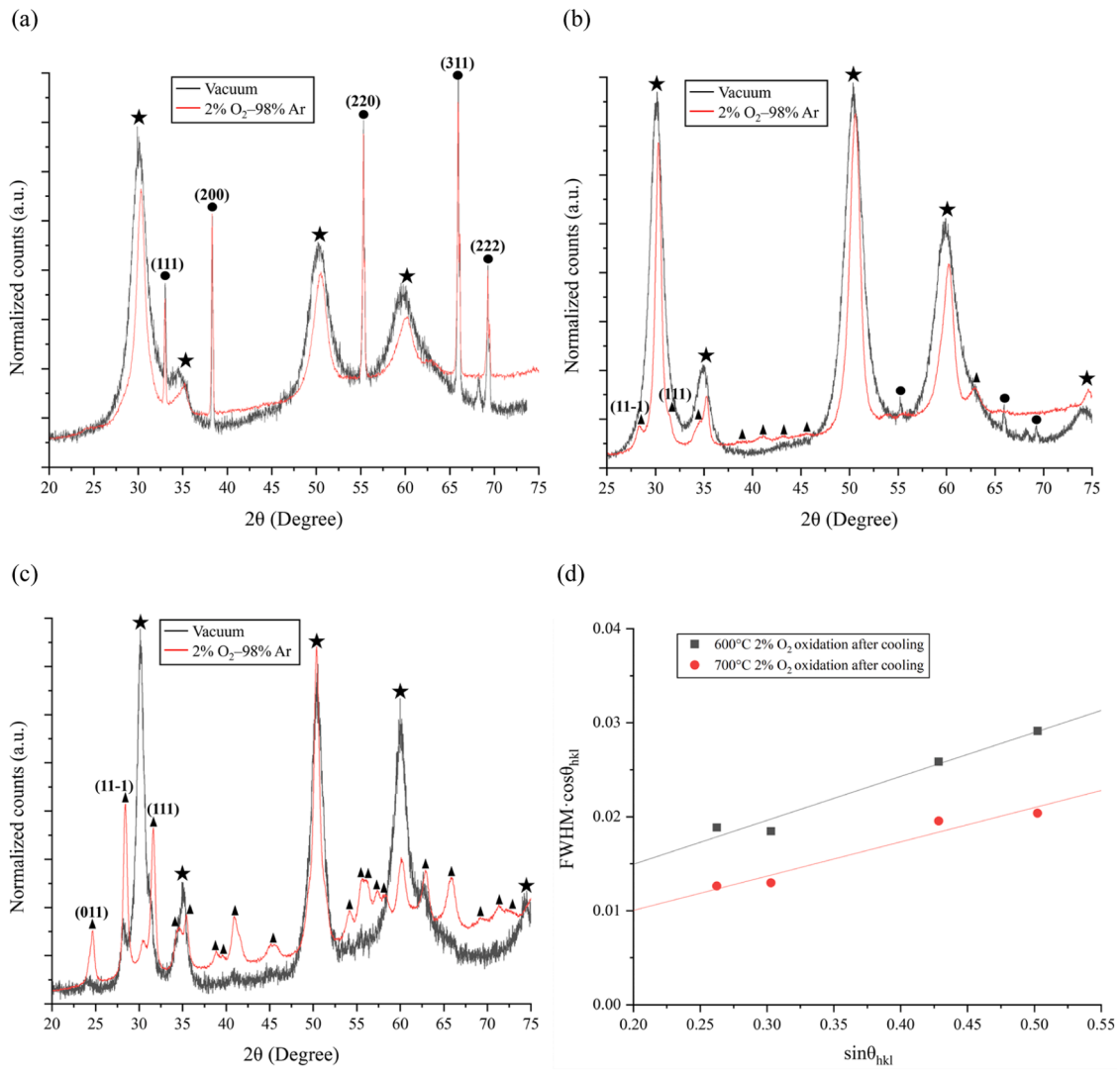


Fig. 13. Phase evolution of ZrC samples under thermal exposure in vacuum (this study) and comparison with high oxygen pressure 2 % O_2 (reproduced from [17] with permission). (a–c) Normalized XRD patterns of samples subjected to isothermal exposure in vacuum (this study) and 2 % O_2 (reproduced from [17] with permission) at (a) 600 °C, (b) 700 °C, and (c) 800 °C. ●: ZrC ★: c/t-ZrO_2 ▲: m-ZrO_2 (d) Williamson–Hall plot of c-ZrO_2 thermally grown in 2 % O_2 [17], used to estimate crystallite sizes and microstrain.

determines whether the oxide remains stabilized in the cubic/tetragonal form or transforms to the monoclinic phase upon cooling.

By using the Williamson-Hall plot, we calculated the crystallite size and microstrain for the c-ZrO_2 phase and compared them with vacuum-grown oxide. At 600 °C, 2 % O_2, the crystallite size (L) is around 28 nm with microstrain 1 %. The size is significantly larger than vacuum-grown oxide (12 nm) at the same temperature with lower microstrain. At 700 °C, 2 % O_2, the L is approximately 55 nm and ε is 1 %. This crystallite size is also significantly larger than vacuum-grown oxide (16 nm). While at 800 °C, 2 % O_2, only a limited amount of c-ZrO_2 remains in the outer scale, with most of the oxide already transformed into monoclinic phase (Fig. 13(c)). These results demonstrate that crystallite size, in addition to cooling conditions, strongly influences phase stabilization and transformation in zirconia scales. A comprehensive summary of oxide scales formed under oxygen-limited and oxygen-rich environments across a range of temperatures is presented in Table 1.

4. Conclusions

This study investigates the behavior of SPS-sintered zirconium carbide (chemical composition: $ZrC_{0.94}O_{0.05}$) at elevated temperatures under vacuum (5×10^{-2} Pa) over sustained time frames, including both isothermal exposure and cooling conditions. To the best of our knowledge, we present the first in-situ tracking of thermally grown oxide formation on SPS-sintered zirconium carbide in vacuum under isothermal temperature range 400–800 °C, and systematically monitored the phase stability of the scales as a function of cooling temperature. Five main conclusions are as follows:

(1) A single-layer nanocrystalline zirconia–carbon composite scale forms under oxygen-limited conditions, which is distinct from the double-layer structure typically observed under high oxygen pressures. The single-layer scale exhibits lattice microstrain and mosaicity, with observable oxidation front stripes and a probable oxycarbide region.
(2) Under oxygen-limited conditions, carbon remains solid for extended durations in the oxide scale, preventing the formation of through-thickness cracks at 600 °C and 700 °C. At 700 °C, in-plane cracks develop due to zirconia growth, while at 800 °C, pronounced grain boundary cracking is identified.
(3) In-situ XRD results reveal direction-dependent intensity variations in ZrC diffraction peaks during isothermal exposure at

Table 1
Summary of oxide scales formed under oxygen-rich and oxygen-limited environments after isothermal oxidation for 10,800 s, followed by cooling to room temperature.

	Temp (°C)	Oxide scale structure	Crack morphologies	Phase of Zirconia in the scale surface	c-ZrO_2 crystallite size (nm)	Oxycarbide region thickness (nm)
Vacuum (Oxygen-limited)	400	No coherent oxide scale (Pronounced XRD reduction in ZrC (220) plane)	–	–	–	–
	600	Single-layer (13.45 ± 0.74 μm)	Limited cracks in oxide scale (Fig. 9 (b))	c-ZrO_2 dominant (Fig. 9(a))	12.2	70–80 adjacent to Zr–C–O layer (Fig. 4 (b))
	700	Single-layer (33.85 ± 0.85 μm)	In-plane cracks in oxide scale (Fig. 10 (b))	c-ZrO_2 dominant (Fig. 10(a))	16.1	–
	800	Single-layer and grain boundary cracking	Grain boundary cracks in ZrC surface (Fig. 11(d))	c-ZrO_2 with minor t-ZrO_2 and m-ZrO_2 (Fig. 11(b))	57.1	–
2 %O_2–98 %Ar (Oxygen-rich) [17]	600	Double-layer (Inner layer 3.85 ± 0.49 μm, and outer layer 4.74 ± 0.76 μm)	Through-thickness & in-plane cracks in oxide scale	Major c-ZrO_2 with minor t-ZrO_2	27.5	20–30 adjacent to Zr–C–O layer
	700	Double-layer (Inner layer 15.05 ± 0.93 μm, and outer layer 71.80 ± 4.00 μm)	Through-thickness & in-plane cracks in oxide scale	Major c-ZrO_2 with minor t-ZrO_2 and m-ZrO_2	55.1	–
	800	Double-layer and grain boundary cracking	Through-thickness & in-plane cracks in oxide scale + Grain boundary cracks in ZrC surface	Major m-ZrO_2	– Transform mostly to m-ZrO_2	–

400 °C. Notably, the ZrC (220) reflection exhibits pronounced intensity reduction, which may indicate a higher susceptibility of this crystallographic plane to defect accumulation.

(4) Temperature and crystallite size both govern the vacuum-grown oxide scale phase transformation and stability. Isothermal experiments alone do not induce monoclinic transformation; it occurs primarily during cooling. m-ZrO_2 formation occurs when crystallite size exceeds a critical threshold, and during cooling at around 450–350 °C. This transformation temperature is substantially lower than the 950–1050 °C cooling range typically reported for the tetragonal-to-monoclinic transformation in coarse-grained undoped zirconia.

(5) Crystallite growth under sufficient oxygen supply is more pronounced than in vacuum, which explains the dominant monoclinic zirconia phase observed in oxygen-rich scales after cooling, compared with mostly fluorite-like zirconia structure in vacuum-grown scales.

These findings highlight the combined importance of temperature, cooling, and crystallite size in controlling phase transformations, structural evolution, and scale morphology in zirconium carbide systems, and advance the mechanistic understanding of ZrC oxidation under constrained oxygen environments.

CRediT authorship contribution statement

Yun-Ching Lin: Writing – review & editing, Writing – original draft, Visualization, Validation, Methodology, Investigation, Formal analysis, Data curation, Conceptualization. **Lars Bannenberg:** Validation, Resources, Methodology. **Amy Navarathna:** Validation, Investigation. **Hyun-Sik Kim:** Validation, Resources, Investigation. **Vera Popovich:** Writing – review & editing, Validation, Supervision, Resources.

Declaration of competing interest

The authors declare that they have no known competing financial interests or personal relationships that could have appeared to influence the work reported in this paper.

Acknowledgements

The authors gratefully acknowledge Rinze Benedictus and Yinglu Tang (Department of Aerospace Structures and Materials, Faculty of Aerospace Engineering, Delft University of Technology) for their valuable discussions and insightful feedback, which enriched this study. The authors also thank Xavier Le Coz (HORIBA Application Laboratory) for performing the elemental analyses using the elemental infrared analyzer (EMIA) and elemental gas analyzer (EMGA).

Supplementary materials

Supplementary material associated with this article can be found, in the online version, at doi:10.1016/j.oceram.2026.101061.

References

[1] G.R. Peterson, R.E. Carr, E.E. Marinero, Zirconium carbide for hypersonic applications: opportunities and challenges, Materials (Basel) 16 (18) (2023) 6158.
[2] A. Ul-Hamid, Microstructure, properties and applications of Zr-carbide, Zr-nitride and Zr-carbonitride coatings: a review, Mater. Adv. 1 (2020) 1012–1037.
[3] P. Yang, F. Peng, X. Xiao, J. Chen, H. Long, R. He, W. Liang, L. Ran, P. He, Sintering pure polycrystalline zirconium carbide ceramics with enhanced mechanical properties under high-pressure and high-temperature, J. Eur. Ceram. Soc. 45 (2025) 117115.
[4] L.N. Grossman, High-temperature thermophysical properties of zirconium carbide, J. Am. Ceram. Soc. 48 (5) (1965) 236–242.
[5] R.E. Taylor, Thermal conductivity of zirconium carbide at high temperatures, J. Am. Ceram. Soc. 45 (7) (1962) 353–354.
[6] Y. Katoh, G. Vasudevamurthy, T. Nozawa, L.L. Snead, Properties of zirconium carbide for nuclear fuel applications, J. Nucl. Mater. 441 (2013) 718–742.
[7] S. Hamilton, N.D. Jerred, R. Scott, M. Bachhav, T. Yao, V.M. Miller, Diffusion study of uranium mononitride/zirconium carbide composite for space nuclear propulsion, J. Nucl. Mater. 583 (2023) 154535.
[8] C. Yan, P. Luo, J. Zhang, Z. Zhao, R. Liu, Ablation behavior of Cf/ZrC–SiC ultra–high temperature ceramic composites in oxyacetylene torch and plasma wind tunnel, Mater. Today Commun. 41 (2024) 110477.
[9] G. Yang, Y. Xiang, T. Poirier, N. Malmir, T. Yao, N. Churi, B. Taylor, J.H. Edgar, D. Lin, S. Lei, Extrusion-based additive manufacturing of zirconium carbide for nuclear fuel cell structures, Ceram. Int. 51 (2025) 252–258.
[10] S. Uzun, Comprehensive analysis of nuclear clad materials: neutronics, radiation shielding, and modal assessment, Nucl. Eng. Des. 428 (2024) 113510.
[11] S. Shimada, T. Ishil, Oxidation kinetics of zirconium carbide at relatively low temperatures, J. Am. Ceram. Soc. 73 (10) (1990) 2804–2808.
[12] L. Charpentier, M. Balat-Pichelin, D. Sciti, L. Silvestroni, High temperature oxidation of Zr- and Hf-carbides: influence of matrix and sintering additive, J. Eur. Ceram. Soc. 33 (2013) 2867–2878.

[13] C. Gasparrini, R. Podor, D. Horlait, R. Chater, W.E. Lee, Zirconium carbide oxidation: Maltese cross formation and interface characterization, Oxid. Met. 88 (2017) 509–519.
[14] S. Shimada, M. Yoshimatsu, M. Inagaki, S. Otani, Formation and characterization of carbon at the ZrCZrO_2 interface by oxidation of ZrC single crystals, Carbon 36 (7–8) (1998) 1125–1131.
[15] S. Shimada, Oxidation and mechanism of single crystal carbides with formation of carbon, J. Ceram. Soc. Jpn. 109 (1267) (2001) S33–S42.
[16] B. Ma, W. Han, E. Guo, Oxidation behavior of ZrC-based composites in static laboratory air up to 1300 °C, Int. J. Refract. Met. Hard Mater. 46 (2014) 159–167.
[17] Y.-C. Lin, R. Huizenga, H.-S. Kim, H. Brouwer, A.M. Armaki, V. Popovich, Y. Tang, Oxidation fronts and oxide scale growth modeling in spark plasma sintered ZrC ultra-high temperature ceramic, J. Eur. Ceram. Soc. 46 (2026) 117976.
[18] Y.-C. Lin, H. Brouwer, V. Popovich, Y. Tang, Three-stage oxidation kinetics and passivation mechanism of spark plasma sintered ZrC ultra-high temperature ceramic, J. Eur. Ceram. Soc. 46 (2026) 117757.
[19] D. Gozzi, M. Montozzi, P.L. Cignini, Oxidation kinetics of refractory carbides at low oxygen partial pressures, Solid State Ionics 123 (1999) 11–18.
[20] X.-M. Hou, K.-C. Chou, Investigation of the effects of temperature and oxygen partial pressure on oxidation of zirconium carbide using different kinetics models, J. Alloys Compd. 509 (2011) 2395–2400.
[21] U.S. Standard Atmosphere, 1976, National Oceanic and Atmospheric Administration (NOAA), Washington, DC, USA, 1976.
[22] T.J. Nijdam, L.P.H. Jeurgens, W.G. Sloof, Effect of partial oxygen pressure on the initial stages of high-temperature oxidation of γ-NiCrAl alloys, Mater. High Temp. 20 (3) (2003) 311–318.
[23] M. Sattari, H. Hooshyar, J. Liske, T. Jonsson, The influence of oxygen partial pressure on the base oxide of chromia forming steels: the story prior to breakaway oxidation, Corros. Sci. 213 (2023) 110959.
[24] S.I. Moseenkov, V.L. Kuznetsov, N.A. Zolotarev, B.A. Kolesov, I.P. Prosvirin, A. V. Ishchenko, A.V. Zavorin, Investigation of amorphous carbon in nanostructured carbon materials (a comparative study by TEM, XPS, Raman spectroscopy and XRD), Materials (Basel) 16 (3) (2023) 1112.
[25] S. Shimada, M. Nishisako, M. Inagaki, Formation and microstructure of carbon-containing oxide scales by oxidation of single crystals of zirconium carbide, J. Am. Ceram. Soc. 78 (1) (1995) 41–48.
[26] S. Shimada, TEM observation of the ZrC/ZrO_2 interface formed by oxidation of ZrC single crystals, J. Mater. Synth. Process. 6 (3) (1998) 191–195.
[27] S.-L. Shang, S. Lin, M.C. Gao, D.G. Schlom, Z.-K. Liu, Ellingham diagrams of binary oxides, APL Mater. 12 (8) (2024).
[28] L. Backman, E.J. Opila, Thermodynamic assessment of the group IV, V and VI oxides for the design of oxidation resistant multi-principal component materials, J. Eur. Ceram. Soc. 39 (5) (2019) 1796–1802.
[29] N. Koide, T. Marumo, Y. Arai, M. Hasegawa, T. Nishimura, R. Inoue, Degradation of carbon fiber-reinforced ultra-high-temperature ceramic matrix composites at extremely high temperature using arc-wind tunnel tests, J. Mater. Sci. 57 (42) (2022) 19785–19798.
[30] C. Gasparrini, R.J. Chater, D. Horlait, L. Vandeperre, W.E. Lee, Zirconium carbide oxidation: kinetics and oxygen diffusion through the intermediate layer, J. Am. Ceram. Soc. 101 (2018) 2638–2652.
[31] S. Shimada, M. Inagaki, M. Suzuki, Microstructural observation of the ZrC/ZrO_2 interface formed by oxidation of ZrC, J. Mater. Res. 11 (10) (1996) 2594–2597.
[32] A. Kucheryavaya, Z. Lenčéš, P. Šajgalík, H. Harmuth, Zirconium oxycarbides and oxycarbonitrides: a review, Int. J. Appl. Ceram. Technol. (2022) 1–22.
[33] S. Shimada, Interfacial reaction on oxidation of carbides with formation of carbon, Solid State Ionics 141-142 (2001) 99–104.
[34] E. Osei-Agyemang, J.-F. Paul, R. Lucas, S. Foucaud, S. Cristol, A.-S. Mamede, N. Nuns, A. Addad, Structure and energetics of ZrC(100)||c-ZrO_2(001) interface: a combination of experiments, finite temperature molecular dynamics, periodic DFT and atomistic thermodynamic modeling, Ceram. Int. 48 (15) (2022) 21327–21343.
[35] E. Osei-Agyemang, J.-F. Paul, R. Lucas, S. Foucaud, S. Cristol, A.-S. Mamede, N. Nuns, A. Addad, Characterizing the ZrC(111)/c-ZrO_2(111) hetero-ceramic interface: first principles DFT and atomistic thermodynamic modeling, Molecules 27 (9) (2022) 2954. Art. no. 2954.
[36] P.M. Kelly, L.R.F. Rose, The martensitic transformation in ceramics—Its role in transformation toughening, Prog. Mater. Sci. 47 (5) (2002) 463–557.
[37] R.H.J. Hannink, P.M. Kelly, B.C. Muddle, Transformation toughening in zirconia-containing ceramics, J. Am. Ceram. Soc. 83 (3) (2000) 461–487.
[38] R.C. Garvie, The occurrence of metastable tetragonal zirconia as a crystallite size effect, J. Phys. Chem. 69 (4) (1965) 1238–1243.
[39] E. Djurado, P. Bouvier, G. Lucazeau, Crystallite size effect on the tetragonal–monoclinic transition of undoped nanocrystalline zirconia studied by XRD and Raman spectrometry, J. Solid State Chem. 149 (2) (2000) 399–407.
[40] S. Shukla, S. Seal, Mechanisms of room temperature metastable tetragonal phase stabilisation in zirconia, Int. Mater. Rev. 50 (1) (2005) 45–64.
[41] Y.C. Lin, H. Brouwer, V. Popovich, Spark plasma sintered zirconium carbide oxidation mechanisms under different temperatures and oxygen partial pressures, in: "Ultra-High Temperature Ceramics: Materials for Extreme Environment Applications VI", ECI Symposium Series, 2024.